Structural and magnetic properties of thin cobalt films with mixed hcp and fcc phases

Gauravkumar Patel [1,2] Fabian Ganss,[1] Ruslan Salikhov [1] Sven Stienen,[1] Lorenzo Fallarino,[1,3] Rico Ehrler,[4]
Rodolfo A. Gallardo,[5] Olav Hellwig [1,4] Kilian Lenz [1] and Jürgen Lindner [1]

[1]*Helmholtz-Zentrum Dresden–Rossendorf, Institute of Ion Beam Physics and Materials Research,
Bautzner Landstraße 400, 01328 Dresden, Germany*
[2]*Faculty of Physics, Dresden University of Technology, D-01062 Dresden, Germany*
[3]*CIC energiGUNE, Parque Tecnológico de Álava, Albert Einstein 48, 01510 Vitoria-Gasteiz, Spain*
[4]*Institute of Physics, Chemnitz University of Technology, 09107 Chemnitz, Germany*
[5]*Departamento de Física, Universidad Técnica Federico Santa María, Avenida España 1680, 2390123 Valparaíso, Chile*

Cobalt is a magnetic material that finds extensive use in various applications, ranging from magnetic storage to ultrafast spintronics. Usually, it exists in two phases with different crystal lattices, namely in hexagonal-close-packed (hcp) or face-centered-cubic (fcc) structure. The crystal structure of Co films significantly influences their magnetic and spintronic properties. We report on the thickness dependence of the structural and magnetic properties of sputter-deposited Co on a Pt seed layer. It grows in an hcp lattice at low thicknesses, while for thicker films it becomes a mixed hcp-fcc phase due to a stacking fault progression along the growth direction. The x-ray-based reciprocal space map technique has been employed to distinguish and confirm the presence of both phases. Moreover, the precise determination of Landé's g-factor by ferromagnetic resonance provides valuable insights into the structural properties. In our detailed experiments, we observe that a structural variation results in a nonmonotonic variation of the magnetic anisotropy along the thickness. This careful study reveals the fundamental physics, but also provides important insight for potential applications of thin Co films with perpendicular magnetic anisotropy.

I. INTRODUCTION

Cobalt is one of the most popular materials for spintronic applications due to its attractive magnetic properties, including high saturation magnetization and large uniaxial magnetic anisotropy [1–3]. Thus, Co-based systems are used for data storage in hard disk drives [4] as well as in modern data-processing concepts [5]. They are also promising candidates for high-performance and energy-efficient electronic devices [6]. Furthermore, cobalt's versatility, its compatibility with various fabrication techniques, and its ability to be deposited on a wide range of materials [7] makes it a valuable candidate for spintronic research and application [8–10].

The magnetic properties of thin-film Co depend significantly on the crystal structure. Co exists in hexagonal-close-packed (hcp) or face-centered-cubic (fcc) phases or even in a mixture of both [11–15]. Therefore, the choice of substrate [16–21], seed layer [22–28], growth temperature [11], and deposition rate [29] can influence the resulting film's structural and magnetic properties. Furthermore, the growth of Co on a Pt seed remains a topic of controversy [30–32], with the resulting phases being highly sensitive to the growth parameters [30].

In the hcp stacking (ABABAB...), Co has a low stacking fault energy [14,33]. This often leads to small fractions of a metastable fcc structure with ABCABC... stacking within the hcp Co [28,34,35]. (The letters A, B, and C represent the conventional stacking sequence of close-packed atomic planes.) The stacking faults either originate from transitions of hexagonal AB stacking to hexagonal CB stacking, where only a single atomic sheet (of orientation B) is in an fcc environment (e.g., ABABCBCB), or through deformation faults, where an AB stacking changes into a CA stacking, and two neighboring atomic sheets (B and C) are in an fcc environment (e.g., ABABCACA) [11,12,36,37]. Previous studies have shown that the probability of obtaining a stacking fault depends on the faults in the previous three atomic layers [11]. This implies that once a crystal starts growing with an fcc stacking fault, subsequent layers progressively take on this fcc phase contribution.

Detecting stacking faults in thin Co films using conventional x-ray diffraction techniques (XRD) is challenging due to the low initial density of stacking faults and the broadening of diffraction peaks caused by the presence of local strains [12]. Moreover, distinguishing between the Bragg diffraction peaks of hcp Co (0002) and fcc Co (111) with almost the same lattice plane spacing can be difficult in thin films due to broadening by the limited coherence length. As a result, the presence of the fcc phase is often overlooked or neglected, and an hcp phase is assumed without detailed structural characterization [38–43]. Given the distinct magnetic properties displayed by hcp and fcc Co phases, a comprehensive understanding of magnetic characteristics in Co films with mixed hcp and fcc phases, caused by stacking faults during growth, is currently elusive. Therefore, it is imperative to conduct a thorough investigation of Co films' crystal structure and magnetic properties across various thickness ranges.
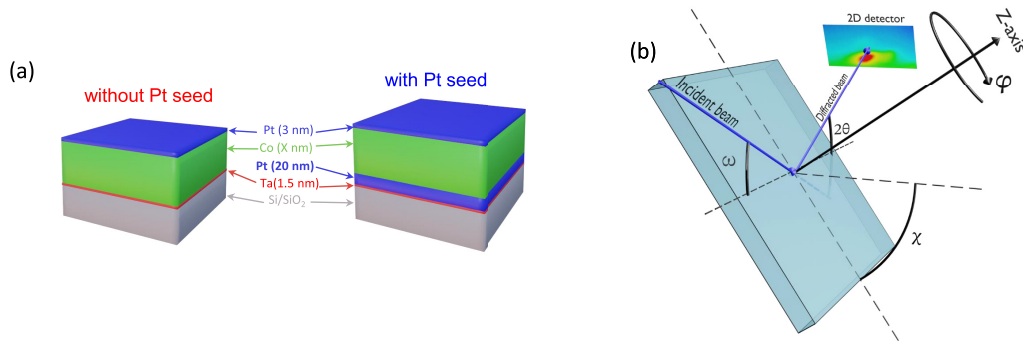
FIG. 1. (a) Sketches of the sample stack with and without the 20 nm Pt seed layer. The Co thickness X was varied between 4 and 110 nm. (b) A schematic diagram of the RSM measurement technique as applied in this study.

In this study, we present two distinct thickness series of Co films. One series was deposited on a Pt (111) seed layer, while the other was deposited without it. Both sets of films were produced using dc magnetron sputtering with a thin amorphous Ta adhesion layer on Si/SiO$_2$ substrates. The Co films with the Pt seed layer exhibit an hcp crystal structure with an increasing fraction of fcc content as the Co thickness increases. This mixed-phase structure in the Co films results in nonmonotonic variations in their magnetic properties with changing thickness, along with the presence of inhomogeneous magnetic anisotropy. We propose the use of XRD reciprocal space mapping together with measurements of Landé g-factor to distinguish between hcp and fcc phases of Co.

II. EXPERIMENTAL DETAILS

The Co films were fabricated at room temperature by dc magnetron sputtering in an ultrahigh-vacuum system (AJA INTERNATIONAL ATC2200) with a base pressure of 10^{-7} mbar. The Ar pressure was kept at 4×10^{-3} mbar during the deposition, and the Ar flow rate was fixed to 25 sccm. Si (001) wafers with a 100-nm-thick thermally oxidized SiO$_2$ surface layer were used as substrates. During the deposition, the substrate was rotated at about 60 rpm. Prior to the sample fabrication, the sputter rate of each material was calibrated using x-ray reflectivity (XRR). A 1.5-nm-thick Ta layer was deposited onto the substrates for better adhesion. Two different thickness series of Co were then fabricated with thicknesses ranging from 4 to 110 nm. One series was directly grown on the Ta adhesion layer, and the other series was grown on an additional 20-nm-thick Pt seed layer, which is enough to have bulklike structural properties for Pt. In the following, the thickness series on top of the Pt seed will be referred to as "with Pt seed," whereas the other thickness series will be referred to as "without Pt seed," as depicted in Fig. 1(a). The Pt seed layer serves to induce a crystalline texture in the Co film [41,42]. All samples from both series are capped by 3 nm of Pt to prevent oxidation at air.

For the structural characterization, XRD $\theta/2\theta$ scans, reciprocal space map (RSM), as well as rocking curve (RC) measurements were performed on a RIGAKU SMARTLAB thin-film four-circle x-ray diffractometer. The instrument uses a parallel beam of Cu $K\alpha$ radiation and is equipped with a HYPIX-3000 two-dimensional semiconductor detector.

An RSM measurement is a very powerful technique to unambiguously identify the phases [47,48]. It records the diffracted intensity while scanning both the diffraction angle (2θ) and the sample tilt (typically an offset in ω, in this case χ). Please refer to Fig. 1(b) for a schematic that shows the measurement geometry. The purpose, in general, is to map a selected region of a two-dimensional cross-section of reciprocal space, which is then compared to a modeled reciprocal lattice and analyzed further. The method we employed makes use of the 2D detector by transforming the coordinates of the detector pixels into 2θ and χ. The intensity is color-coded in the contour plots in Fig. 3, and we have added black contour lines of equal intensity to highlight the peaks. RSMs are usually transformed into reciprocal space coordinates for further analysis. However, for better visualization we plot them on the original angular axes here.

The static magnetic properties were evaluated at ambient temperature using a commercial MICROSENSE EZ7 vibrating sample magnetometer (VSM). Hysteresis loops with in-plane (IP) and out-of-plane (OOP) field were measured. The saturation magnetization (M_s) was determined with field in the OOP direction. The hysteresis loops were subsequently normalized for further analysis.

Magnetic domain imaging was performed by a BRUKER DIMENSION ICON magnetic force microscope (MFM) using a double-pass tapping-lift mode with a lift height of 30 nm. The contrast presented was derived from the phase shift observed during the second pass subsequent to the topographic measurement. This allowed us to probe the magnetic field gradient along the vertical direction. Commercial PPP-LM-MFMR (Point Probe Plus Magnetic Force Microscopy–Low Momentum–Reflex Coating) tips from NANOSENSORS were used with a magnetization of 150 kA/m and approximately 25 mT coercivity. Prior to scanning, the MFM tips were magnetized vertically using a permanent magnet.

The dynamic magnetic properties were measured by broadband vector network analyzer ferromagnetic resonance (VNA-FMR) using an AGILENT E8364B VNA. The sample was placed flip-chip onto a coplanar waveguide, and the complex microwave transmission parameter (S_{21}) was recorded as the FMR signal in field-sweep mode at fixed frequencies. The magnetic field (H) was swept between ± 2.2 T in the OOP direction. At resonance, the precession of the magnetic moments absorbs microwave energy, resulting in a resonance
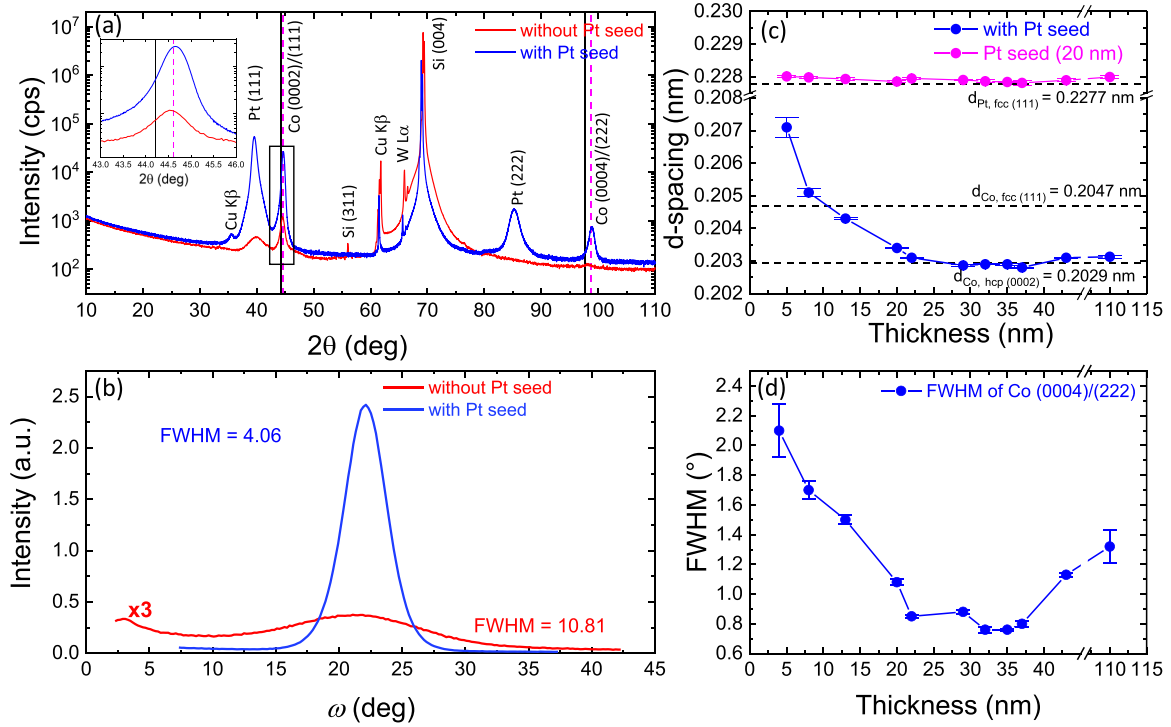
FIG. 2. (a) $\theta/2\theta$ XRD scans of the 35-nm-thick Co film with the Pt seed layer (blue curve) and without (red curve). The vertical black solid line and the magenta dashed line indicate the peak positions for fcc Co (111) (or Co (222)) and hcp Co (0002) (or Co (0004)), respectively. The inset magnifies the Co (0002)/(111) peak region indicated by the black rectangle. A small bump around $2\theta = 40°$ in the red curve originates from the Pt cap layer. The Cu and W spectral lines of the x-ray source are labeled. The slight mismatch observed in the XRD data for the Si (004) substrate peaks in the two different samples is caused by the miscut of the Si wafer surface and the alignment routine referring to the sample surface. Since the films are grown on a 100-nm-thick thermally oxidized surface of Si and have a much broader texture, the exact orientation of the Si lattice does not significantly affect the film reflections, and it can be disregarded, as Fig. S1 [44] demonstrates in more detail. (b) Rocking curve measurements for a Co thickness of 35 nm around the Co (0002)/(111) Bragg peak. For Co without Pt seed (red curve), the measured intensity is scaled by a factor of 3. (c) d-spacing of the Co (blue line) and Pt (magenta line) lattice planes as a function of the Co thickness. The dashed horizontal lines indicate reference d-spacing values for the hcp [45] and fcc [46] phases of Co. (d) FWHM of the Co (0004)/(222) diffraction peak for the thickness series with Pt seed.

line in S_{21}. Two exemplary raw FMR spectra are shown in Fig. S2 of the Supplemental Material [44].

III. EXPERIMENTAL RESULTS

A. Structural characterization

Figure 2(a) shows the XRD $\theta/2\theta$ scans in the angular range $10° \leqslant 2\theta \leqslant 110°$ for the 35 nm Co film with Pt seed (blue curve) and without Pt seed (red curve). The scans exhibit well-defined diffraction peaks corresponding to the lattice planes of Si (004) from the substrate, and Pt (111) and Pt (222) from the seed layer. This seed layer grows in an fcc structure with a (111)-oriented fiber texture, and it supports the textured growth of the Co film. Corresponding diffraction peaks of Co are visible in Fig. 2(a) as well. The Co film grown without the Pt seed layer develops only a faint texture as indicated by its broad, low intensity diffraction peaks. Figure 2(b) shows the RC measurements exemplarily for the 35-nm-thick Co film with and without the Pt seed. The full width at half-maximum (FWHM) of the RC is a measure of the distribution of the crystal orientation in the film. The RC of the sample without Pt seed is rather broad (FWHM = 10.81°) and of low intensity, hence we can infer that the Co thickness series without

Pt seed grows in a rather broad angular distribution, whereas the samples from the series with Pt seed grow well-textured and the orientation distribution is narrower (FWHM = 4.06°). Such a fiber texture in Co gives rise to perpendicular magnetic anisotropy (PMA). In conclusion, the same thickness of Co grown under the same conditions but with a different under-layer will not necessarily have the same textural quality and magnetic properties.

Figure 2(c) shows the lattice plane distance d of Co with Pt seed (blue curve), which has been calculated from the angular position of the Co (0002)/(111) reflections as a function of the Co thickness. The d-spacing shows an inverse dependence on the thickness with a saturation towards the (0002) lattice plane spacing of hcp Co at higher thicknesses. This indicates that the lattice of Co experiences a compressive strain in the film plane at the interface and consequently expands along the surface normal. This strain relaxes as the growth progresses, resulting in a strain gradient. The strain appears as a result of the lattice parameter mismatch between the Pt and Co crystals at the interface and relaxes via the occurrence of misfit dislocations and stacking faults. For thicker films, as strain relaxes, the d-spacing approaches a bulklike value [45]. However, at higher thickness (43 and 110 nm), a surprising slight increase of the
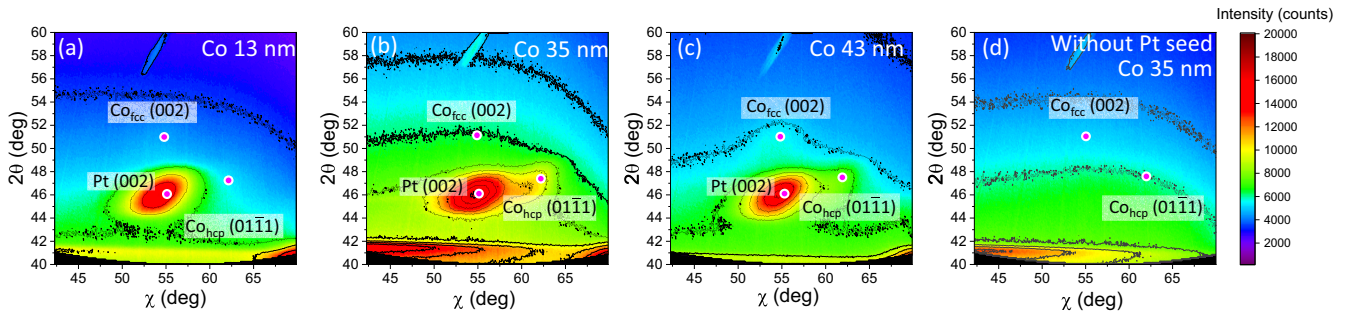
FIG. 3. Reciprocal space maps with black contour lines of (a) 13 nm, (b) 35 nm, (c) 43-nm-thick Co with Pt seed, and (d) a 35-nm-thick Co film without Pt seed. Magenta dots denote the angles where the peaks of ideal fcc (002) [denoted as "Co_{fcc} (002)"] or hcp (01$\bar{1}$1) [denoted as "Co_{hcp} (01$\bar{1}$1)"] lattices are expected, respectively. The central red region in (a), (b), and (c) stems from the 20 nm Pt seed layer.

d-spacing is observed, which will be discussed later in this section. We note a quasiconstant *d*-spacing of the Pt seed layer (magenta curve) for the whole thickness series. This confirms the robustness and reproducibility of our fabrication process and that the observed increase of the Co *d*-spacing at higher thicknesses is not due to instrumental uncertainty.

Usually, the lattice structure of Co films on a Pt seed layer is assumed to be hexagonal—especially when a detailed structural characterization was not performed [35,38–43]. Note that the angular peak positions of the cubic (fcc) Co phase and the hexagonal (hcp) Co phase are $2\theta = 44.22°$ and $44.61°$, respectively. They are marked in Fig. 2(a) by the solid black and dashed magenta lines [45,46] and also displayed as an inset image with fine angular resolution. Additionally, the Co films are also strained, as can be seen in Fig. 2(c). Thus, it is in general not straightforward to distinguish between both phases of Co just from the normal XRD $\theta/2\theta$ scans as both Bragg peaks will overlap significantly because of their broadening. However, for the sample discussed in Fig. 2(a), 35 nm Co with Pt seed (blue curve), the peak matches the reference position of hcp Co. Later in this section we will discuss that for this specific sample, the Co has indeed an hcp structure. However, thicker Co films develop a small deviation from a pure hcp phase. The slight increase of the lattice plane spacing in Fig. 2(c) is a first hint of this.

To unambiguously distinguish between the fcc and hcp Co phases, we identified sets of lattice planes that are not parallel to each other for the two phases, and we used RSM to detect and plot them in Fig. 3. The higher intensity in the red-colored central region in Figs. 3(a)–3(c) stems from the fcc (002) lattice planes of Pt. The other two points marked in magenta are reference positions denoting diffraction intensities from the fcc (002) and the hcp (01$\bar{1}$1) lattice planes of Co, respectively. In Fig. 3(a) for 13 nm Co on Pt seed, there is no visible intensity at any of the two Co reference positions. We assume it to be in the hcp phase. Because of the strain, which we observe along the *c*-axis in Fig. 2(c), we would expect the (01$\bar{1}$1) reflection to shift towards lower 2θ and larger χ, but its intensity is too low compared to the background and the spread of the Pt reflection. For an intermediate Co thickness of 35 nm, as shown in Fig. 3(b), there is significant intensity around the hexagonal Co reference position but not around the cubic reference position. Hence, the hcp phase is dominant for intermediate thickness. Increasing the thickness further to 43 nm of Co on Pt seed, as shown in

Fig. 3(c), we find intensity not only around the hcp phase but also around the fcc phase reference position, proving the coexistence of both phases. Below 35 nm, no evidence of the fcc phase is observed. Thus, we assume that the fcc phase is concentrated within the upper part of the Co film, if we exclude postdeposition lattice plane changes. Similarly, when examining a 110 nm Co film deposited on the Pt seed, we also observe the coexistence of both phases [see the Supplemental Material, Fig. S3(c) [44]]. Notably, the intensity ratio of the fcc (002) to the hcp (01$\bar{1}$1) reflection increases from 0.75 for the 43 nm Co film to 0.99 for the 110 nm Co film. However, this does not imply an equal amount of both phases for the 110 nm film. Instead, the relative intensity of the fcc reflection is approximately five times higher than that of the hcp one.

Summarizing the structural analysis, the fcc phase is not observed for Co thicknesses up to 35 nm. This indicates that in the initial growth phase below 35 nm, the number of fcc stacking faults is low and we have a more or less clean hcp phase, while at higher Co thickness the probability of getting fcc stacking faults increases. This advent of stacking faults after an initial, almost ideal hcp growth can be explained by the earlier mentioned effect that the probability for stacking faults depends on already existing stacking faults in the previous three monolayers [11]. Thus, once the stacking faults occur, they keep increasing their presence.

As both phases have very similar diffraction angles in the normal $\theta/2\theta$ scan, the mixed phase results in a single, broadened Co diffraction peak whose FWHM increases at higher Co thickness as shown in Fig. 2(d), though a larger film thickness would typically lead to a smaller FWHM. This behavior is also consistent with the observed increase of the *d*-spacing for the 43- and 110-nm-thick Co films as shown in Fig. 2(c). Both trend changes occurring at about 40 nm Co thickness indicate the increased occurrence of fcc stacking faults. Finally, this structural variation along the thickness of the Co film grown on Pt leads to a variation of the PMA [49–51]. The cubic phase of Co has a lower magnetocrystalline anisotropy than the hexagonal phase. This creates an anisotropy gradient along the film thickness.

In contrast to the above-mentioned thickness series, the RSM of the Co films grown directly on the Ta adhesion layer, as shown in Fig. 3(d), exhibits no Bragg peaks at the respective reference positions. The crystal orientation is spread across a large angular range (FWHM = 10.81°). As a result,
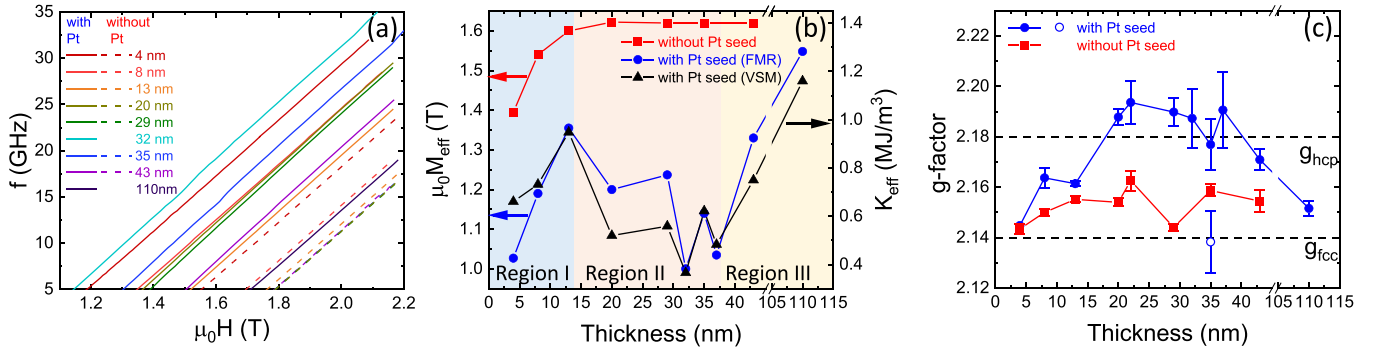
FIG. 4. (a) $f(H)$ plots for both thickness series. The same color indicates the same thickness; solid and dashed lines indicate samples with and without Pt seed, respectively. (b) Effective magnetization ($\mu_0 M_{eff}$) of Co with (blue curve) and without (red curve) Pt seed as well as effective anisotropy (K_{eff}) of Co with Pt seed (black curve) are plotted as functions of the Co thickness. K_{eff} is determined from the area enclosed between in-plane and out-of-plane hysteresis loops in the positive field cycle as highlighted in Fig. 5(a). (c) g-factor of Co with (blue curve) and without (red curve) Pt seed is plotted as a function of the thickness of Co. The horizontal dotted and dashed lines are the references for the g-factors of hcp and fcc phase of Co, respectively.

no significant intensities are recorded in the RSM for any of the two Co phases.

B. Ferromagnetic resonance measurements

Figure 4(a) shows the $f(H)$ plots for both thickness series. The continuous and dotted lines represent the $f(H)$ dependences for films with and without the Pt seed layer, respectively. The frequency modes follow the Kittel resonance equation for thin films saturated in the OOP direction [52,53], namely

$$f = \frac{\gamma}{2\pi}(\mu_0 H_{res} - \mu_0 M_{eff})$$

$$\text{with} \quad \mu_0 M_{eff} = \mu_0 M_s - \frac{2K_{2\perp}}{M_s}, \qquad (1)$$

where $\gamma = g\mu_B/\hbar$ is the gyromagnetic ratio, g is Landé g-factor, μ_B is the Bohr magneton, $\hbar$ is the reduced Planck constant, μ_0 is the vacuum magnetic permeability, M_s is the saturation magnetization, and $K_{2\perp}$ is the first-order uniaxial out-of-plane anisotropy constant, where a positive value indicates an OOP easy axis of magnetization. Fitting all the linear curves in Fig. 4(a) using the Kittel equation, we can determine the effective magnetization $\mu_0 M_{eff}$ and g-factor from the intercept and slope, respectively. Figure 4(b) shows $\mu_0 M_{eff}$ for both thickness series as a function of the Co thickness. At increasing thickness in the series without Pt seed, $\mu_0 M_{eff}$ increases and saturates at thicknesses above 13 nm. As the M_s of all films is almost identical (see Fig. S4 in the Supplemental Material [44]), the behavior of $\mu_0 M_{eff}$ can be understood from the interfacial character of the surface anisotropy, which implicates a reduction of the anisotropy as the thickness of the Co layer increases. However, for Co with Pt seed, $\mu_0 M_{eff}$ shows a rather nonmonotonous behavior upon increasing thickness instead of saturation. To verify the $\mu_0 M_{eff}$ behavior in the FMR measurements, we have measured the related quantity $K_{eff} = \mu_0 M_s^2/2 - K_{2\perp}$ using VSM by determining the area between the in-plane and out-of-plane hysteresis loops for the positive field sweep as depicted as a gray region in Fig. 5(a). As shown in Fig. 4(b), both $\mu_0 M_{eff}$

(from FMR) and K_{eff} (from VSM) exhibit the same characteristic trend as functions of Co thickness.

To understand the nonmonotonous behavior, we divided the whole Co thickness range into three regions. In region (I), below 13 nm, the magnetic anisotropy has a major contribution from the surface anisotropy that decreases at increasing thickness. Hence $\mu_0 M_{eff}$ increases in this region. In region (II), between 13 and 40 nm, the strain caused by the lattice mismatch between the Pt seed and the Co layer relaxes to values characteristic of bulk hcp Co, as evident from Fig. 2(c), and the Co films exhibit an hcp structure without significant fcc stacking faults. The magnetocrystalline anisotropy of the hcp phase of Co is the highest. Hence, the OOP uniaxial anisotropy increases, and thus $\mu_0 M_{eff}$ decreases.

In region (III), between 40 and 110 nm, according to the structural characterization, there is a significant amount of fcc phase within the hcp structure. The contribution of the fcc phase to the uniaxial anisotropy is relatively small [1]. This results in a decrease in the overall magnetic anisotropy for Co thicknesses above 40 nm. As a consequence, $\mu_0 M_{eff}$ increases again. The calculated values of $K_{2\perp}$ for both thickness series are summarized in Fig. S4(b) [44].

Using the fit to the FMR data in Fig. 4(a), the g-factor for both thickness series has been determined and plotted in Fig. 4(c). The g-factor is directly related to the ratio of the orbital to spin magnetic moment [54–57], which depends on the crystal structure.

Although small, the changes of the g-factor extracted from the FMR measurements clearly reflect the structure of the Co films. In Fig. 4(c), the g-factors for bulk fcc and hcp Co [57,58] are marked as horizontal dashed lines for reference. Strain at lower thickness affects the crystal structure and results in a lower g-factor. When the strain releases at higher thickness, the g-factor saturates at the bulk value. Further structural variation, i.e., the coexistence of hcp and fcc phases in very thick films, reduces the g-factor again. Therefore, the sensitivity of the g-factor measurement for the fcc phase can indeed be beneficial in assessing the purity of the hcp phase.

However, some care has to be taken in interpreting the measured g-factor for very thick films. In Fig. 4(c), the g-factor apparently approaches the fcc reference value, while
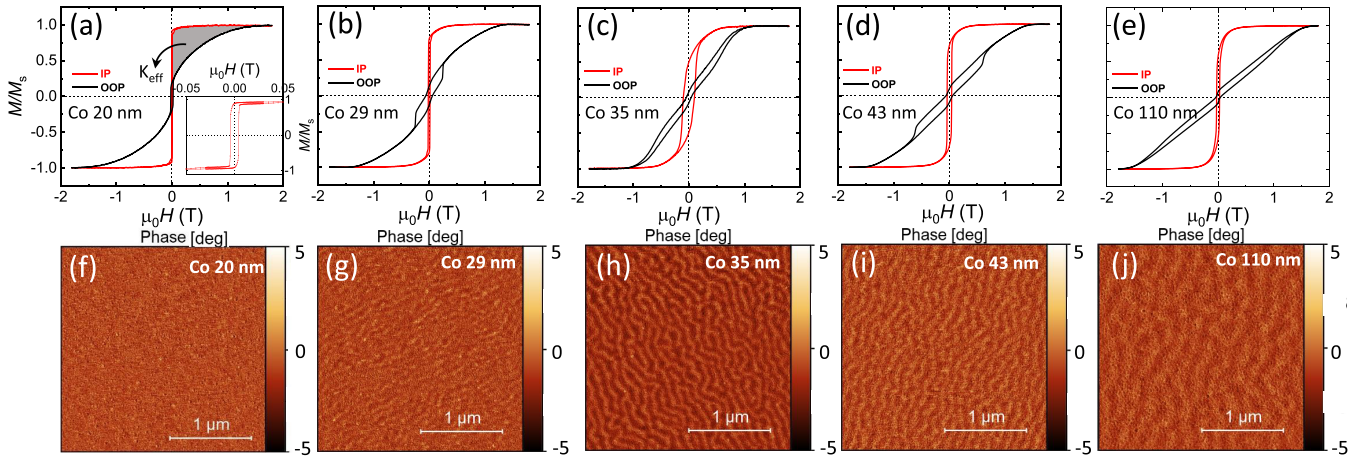
FIG. 5. (a)–(e) In-plane (red) and out-of-plane (black) magnetization reversal (hysteresis) loops measured by VSM at room temperature for selected Co thicknesses with the Pt seed layer. The gray area in the top right quadrant of (a) is used to determine the effective magnetic anisotropy (K_{eff}). K_{eff} is calculated for all samples with Pt seed and plotted in Fig. 4(b). The inset of (a) shows the enlarged IP hysteresis loop for an external field range between ±0.05 T with a field step of 0.5 mT. (f)–(j) Corresponding MFM images taken at remanence after out-of-plane saturation. All the MFM images are plotted with the same color scale, which corresponds to the phase change.

the lattice plane spacing in the thickest films only exhibits a weak trend towards the fcc value [see Fig. 2(c)]. Unlike in the ultrathin film limit, for which exchange will enforce an in-phase precession of all spins across the thickness with the same amplitude, the main FMR mode in a thick film develops a specific profile along the film thickness due to the changes in the magnetic properties along the thickness [40]. The precession amplitude in the latter case will be influenced by the local field within the film, which significantly changes if fcc regions with much smaller magnetic anisotropy are present. In fact, the precession amplitude becomes larger for smaller internal fields and so the mode's response stems to a large extent from those areas. This will in turn lead to an overestimation of the fcc content in FMR measurements of very thick films and thus to a much lower *g*-factor.

The decreasing *g*-factor of films exceeding a thickness of about 40 nm is in good agreement with the appearing fcc reflection in the RSM. From both methods, we conclude that the fcc content occurs to a larger extent in the topmost part of the Co film. This in turn implies that the thicker films exhibit a vertical anisotropy gradient.

To get further insight into the relation between the *g*-factor and the mixed hcp/fcc phase within the Co films, one more sample with a Co thickness of 35 nm on a Pt seed has been fabricated with the same growth parameters except for one: the distance between the target material and the substrate was increased, resulting in a lower kinetic energy of the atoms arriving at the substrate and a lower growth rate. The *g*-factor of this specific sample, instead of approaching the hcp reference line, rather reaches the fcc one, as shown by an open blue circle in Fig. 4(c). To test for an fcc structure, the RSM for this specific sample was measured as well [see Fig. S3(b) of the Supplemental Material [44]]. This indeed confirms a dominant fcc structure. The *g*-factor determined by FMR is in fact sensitive to the different phases of Co and can be used as a complementary measurement technique to RSM. Furthermore, the growth of Co on Pt is very sensitive to the deposition parameters.

In contrast, for the Co thickness series without a Pt seed (red line), the *g*-factor increases initially and saturates between the values for fcc and hcp phase. In this case, the phase determination from x-ray results as discussed in Sec. III A was not possible, and so FMR provides a complementary insight.

C. Magnetostatic characterization

Figures 5(a)–5(e) show magnetic hysteresis loops measured in the IP and OOP geometries for samples grown on Pt seed with different Co thicknesses.

For low Co thicknesses in the range of 4–20 nm, regardless of their OOP surface anisotropy, an IP easy-axis behavior was found. As an example, Fig. 5(a) shows a hysteresis loop for 20-nm-thick Co. The IP magnetization (red line) exhibits a lower saturation field compared to the OOP loop (black line), indicating an IP easy-axis behavior. Furthermore, the IP loop shows a nearly unity remanent magnetization, suggesting the absence of domain states following IP saturation. Figure 5(f) shows the respective MFM image at remanence after OOP saturation. The MFM does not show any domains, indicating an IP magnetization ground state, which is consistent with the loops in Fig. 5(a). Figure 5(b) shows the hysteresis loop of the 29 nm Co film with Pt seed. As the Co thickness increases, the IP single domain state is no longer the energetic ground state. As a result of the competition between magnetic shape anisotropy and magnetocrystalline anisotropy, the ground state of the system changes into a partially OOP tilted stripe-domain state, which is energetically more favorable now. This thickness-dependent transition of magnetization from an IP single-domain state to an OOP stripe-domain state is known as the magnetization reorientation transition [39–41,59–63]. The behavior is typical for magnetic thin films with a quality factor $Q = 2K_{2\perp}/\mu_0 M_s^2 < 1$. Hence, for this thickness-dependent phenomenon, based on energetic arguments in micromagnetic estimations [39,60,61], a critical thickness can be defined as a thickness above which weak stripe-domain structures appear first. At remanence, the critical thickness for small-*Q* materials is given by $d_{cr} \propto$
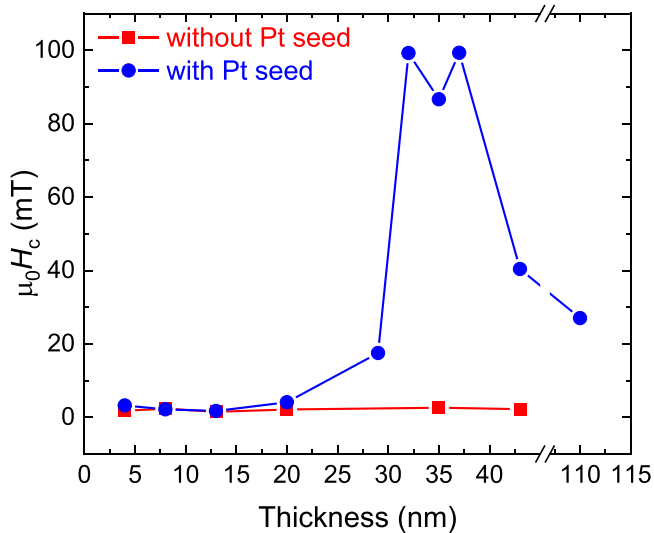
FIG. 6. Coercive field (H_c) of both thickness series as determined from IP hysteresis loops, plotted vs film thickness.

$\sqrt{A/K_{2\perp}}$, where A is the exchange constant. For Co thin-films, d_{cr} ranges between 20 and 40 nm [39]. In our case of Co grown on Pt seed layer, it is about 29 nm. As shown by the MFM image in Fig. 5(g), the tilted stripe domains start to appear as an indication of the magnetization reorientation transition.

Beyond the critical thickness, the behavior of the films changes significantly. Figure 5(c) shows the hysteresis loop of the 35 nm film. From the RSM measurement shown in Fig. 3(b), we learned that the dominant crystal structure is hcp. This has the highest perpendicular magnetic anisotropy, and as a result Fig. 5(h) shows an even more pronounced stripe domain state.

Generally for thin films beyond the critical thickness, the contrast between alternating dark and bright stripes as well as the average stripe period should increase with the film thickness [39]. In our study, however, for 43 nm Co on Pt seed, Fig. 5(i) shows again a weaker stripe domain contrast and a smaller stripe period. Also the area enclosed by the IP hysteresis loop in Fig. 5(d) has decreased again. This trend continues even to the very thick 110 nm Co film, and it is clearly seen in Fig. 5(j) except for the stripe domain period, which increases again due to the larger thickness [64]. These anomalous, nonmonotonous changes in the hysteresis loops and in the MFM stripe domain contrast are also well understood from the coercive field (H_c), as shown in Fig. 6, which increases above d_{cr}, reaches a maximum where the stripe domains are most pronounced, and decreases again for higher thickness as a result of the mixed hcp-fcc phases, which eventually reduce the OOP anisotropy.

As discussed in Sec. III A, we know that both the fcc and the hcp phase of Co coexist in the 43- and 110-nm-thick films. As fcc Co has a lower magnetocrystalline anisotropy [1,65], it reduces the overall OOP anisotropy, and as a result weaker stripe domains are observed again as compared to the 35 nm film.

For the thickness series of Co grown without the Pt seed, the magnetic response is summarized in Fig. 6 as a variation of IP coercive field H_c with film thickness. An almost constant

and very small value of H_c is extracted from the IP hysteresis loops for all thicknesses. As discussed above, the growth of Co without Pt seed results in a relatively poor texture. There is almost no perpendicular anisotropy to compete with the shape anisotropy at any given thickness, and IP magnetization remains the ground state. For direct comparison, the hysteresis loops and MFM images of 35 nm Co without Pt seed are shown in Fig. S5 in the Supplemental Material [44].

IV. CONCLUSION

We have studied two different thickness series of Co films, one of them sputter-deposited directly on a Ta adhesion layer, and the other one on an additional Pt seed layer. We found that Co grown directly on Ta exhibits a poor texture, and its magnetic properties behave monotonically at increasing thickness. On the other hand, the Co thickness series with Pt seed grows initially with an out-of-plane hcp AB-type stacking, but then develops a significant amount of fcc stacking faults at higher thickness as a result of the low stacking fault energy of hcp Co. The probability of stacking faults is low in the initial growth stage, but increases as growth proceeds. At higher thicknesses above 40 nm, the probability of fcc stacking faults increases enough that both fcc and hcp Co phases coexist, according to both RSM and FMR measurements.

The observed crystal structure evolution is consistent with the g-factor variations, where we observed a standard hcp g value up to 35 nm Co thickness, while for thicker films with mixed hcp-fcc phases the g-factor decreases and lies in between the reference values for both phases. A different sample of 35-nm-thick Co fabricated at larger target to substrate distance shows a pure fcc structure in the RSM measurement, which is consistent with the observed g-factor. Hence, we demonstrate that a precisely determined g-factor from FMR can be used complementary to an advanced XRD analysis in order to study such complex changes in the structural and thereby magnetic properties during the growth of magnetic thin films. We find that the structural variation along the thickness causes a nonmonotonous variation of $\mu_0 M_{eff}$ and K_{eff}. To purposely design and fabricate such variations and anisotropy gradients, different methods have been used, such as varying the sputter pressure, temperature, multilayering, or ion-implantation. We demonstrate in our study that such oft-desired anisotropy gradients can also be achieved by using the natural occurrence of stacking faults when increasing the Co thickness. Given the generality of our findings and the simple assumptions we have made, we expect that our work will extend to different materials exhibiting PMA. As a result, we see our article as yet another example of the major relevance of PMA thin films, making them a critical test object that contributes to a more thorough and comprehensive knowledge of basic magnetism.

[1] W. Sucksmith and J. E. Thompson, The magnetic anisotropy of cobalt, Proc. R. Soc. London, Ser. A **225**, 362 (1954).

[2] R. Sbiaa, H. Meng, and S. N. Piramanayagam, Materials with perpendicular magnetic anisotropy for magnetic random access memory, Phys. Status Solidi RRL **5**, 413 (2011).

[3] B. Tudu and A. Tiwari, Recent developments in perpendicular magnetic anisotropy thin films for data storage applications, Vacuum **146**, 329 (2017).

[4] A. Hirohata and K. Takanashi, Future perspectives for spintronic devices, J. Phys. D **47**, 193001 (2014).

[5] P. Monalisha, A. P. S. Kumar, X. R. Wang, and S. N. Piramanayagam, Emulation of synaptic plasticity on a cobalt-based synaptic transistor for neuromorphic computing, ACS Appl. Mater. Interfaces **14**, 11864 (2022).

[6] Z. Guo, J. Yin, Y. Bai, D. Zhu, K. Shi, G. Wang, K. Cao, and W. Zhao, Spintronics for energy-efficient computing: An overview and outlook, Proc. IEEE **109**, 1398 (2021).

[7] A. E. Kaloyeros, Y. Pan, J. Goff, and B. Arkles, Editors' choice—review—cobalt thin films: Trends in processing technologies and emerging applications, ECS J. Solid State Sci. Technol. **8**, P119 (2019).

[8] A. Manchon, J. Železný, I. M. Miron, T. Jungwirth, J. Sinova, A. Thiaville, K. Garello, and P. Gambardella, Current-induced spin-orbit torques in ferromagnetic and antiferromagnetic systems, Rev. Mod. Phys. **91**, 035004 (2019).

[9] T. H. Dang, J. Hawecker, E. Rongione, G. B. Flores, D. Q. To, J. C. Rojas-Sanchez, H. Nong, J. Mangeney, J. Tignon, F. Godel, S. Collin, P. Seneor, M. Bibes, A. Fert, M. Anane, J.-M. George, L. Vila, M. Cosset-Cheneau, D. Dolfi, R. Lebrun *et al.*, Ultrafast spin-currents and charge conversion at 3d-5d interfaces probed by time-domain terahertz spectroscopy, Appl. Phys. Rev. **7**, 041409 (2020).

[10] M. Matthiesen, D. Afanasiev, J. R. Hortensius, T. C. van Thiel, R. Medapalli, E. E. Fullerton, and A. D. Caviglia, Temperature dependent inverse spin hall effect in Co/Pt spintronic emitters, Appl. Phys. Lett. **116**, 212405 (2020).

[11] V. Sokalski, D. E. Laughlin, and J.-G. Zhu, Magnetic anisotropy and stacking faults in Co and $Co_{84}Pt_{16}$ epitaxially grown thin films, J. Appl. Phys. **110**, 093919 (2011).

[12] C. Houska, B. Averbach, and M. Cohen, The cobalt transformation, Acta Metall. **8**, 81 (1960).

[13] J. W. Christian, A theory of the transformation in pure cobalt, Proc. R. Soc. London A **206**, 51 (1951).

[14] R. Su, D. Neffati, J. Cho, Q. Li, J. Ding, H. Wang, Y. Kulkarni, and X. Zhang, Phase transformation induced plasticity in high-strength hexagonal close packed Co with stacking faults, Scr. Mater. **173**, 32 (2019).

[15] J. A. Arregi, J. B. González-Díaz, O. Idigoras, and A. Berger, Strain-induced magneto-optical anisotropy in epitaxial hcp Co films, Phys. Rev. B **92**, 184405 (2015).

[16] B. Gu and H. Wang, Structure and magnetic properties of sputtered fcc Co(111) films grown on a glass substrate, J. Magn. Magn. Mater. **187**, 47 (1998).

[17] C. Mocuta, Growth and magnetism of Co/NiO(111) thin films, Thin Solid Films **336**, 160 (1998).

[18] G. A. Prinz, Stabilization of bcc Co via epitaxial growth on GaAs, Phys. Rev. Lett. **54**, 1051 (1985).

[19] H. Li and B. P. Tonner, Direct experimental identification of the structure of ultrathin films of bcc iron and metastable bcc and fcc cobalt, Phys. Rev. B **40**, 10241 (1989).

[20] J. A. Wolf, J. J. Krebs, Y. U. Idzerda, and G. A. Prinz, Magnetic studies of fcc Co films grown on diamond (abstract), J. Appl. Phys. **76**, 6452 (1994).

[21] G. R. Harp, R. F. C. Farrow, D. Weller, T. A. Rabedeau, and R. F. Marks, Unusual stability of fcc Co(110)/Cu(110), Phys. Rev. B **48**, 17538 (1993).

[22] W. Weber, A. Bischof, R. Allenspach, C. H. Back, J. Fassbender, U. May, B. Schirmer, R. M. Jungblut, G. Guntherodt, and B. Hillebrands, Structural relaxation and magnetic anisotropy in Co/Cu(001) films, Phys. Rev. B **54**, 4075 (1996).

[23] N. Kikuchi, O. Kitakami, S. Okamoto, Y. Shimada, A. Sakuma, Y. Otani, and K. Fukamichi, Influence of 5d transition elements on the magnetocrystalline anisotropy of hcp-Co, J. Phys.: Condens. Matter **11**, L485 (1999).

[24] Y. V. Goryunov, G. G. Khaliullin, I. A. Garifullin, L. R. Tagirov, F. Schreiber, P. Bödeker, K. Bröhl, C. Morawe, T. Mühge, and H. Zabel, FMR studies of magnetic properties of Co and Fe thin films on Al_2O_3 and MgO substrates, J. Appl. Phys. **76**, 6096 (1994).

[25] S. Jomni, N. Mliki, R. Belhi, K. Abdelmoula, M. Ayadi, and G. Nihoul, Face centred cubic cobalt ultrathin-layers in Au/Co(111) multilayers: a study by electron diffraction and by HREM, Thin Solid Films **370**, 186 (2000).

[26] T. Kehagias, P. Komninou, C. Christides, G. Nouet, S. Stavroyiannis, and T. Karakostas, Growth of fcc Co in sputter-deposited Co/Au multilayers with (111) texture, J. Cryst. Growth **208**, 401 (2000).

[27] H. Ardhuin, E. Snoeck, and M.-J. Casanove, Epitaxial growth of magnetic Au/Co/Au sandwiches studied by TEM, J. Cryst. Growth **182**, 394 (1997).

[28] M. Benaissa, P. Humbert, H. Lefakis, J. Werckmann, V. Speriosu, and B. Gurney, Structural characterization of Co in sputtered Ta/Co/Ta thin-film sandwiches, J. Magn. Magn. Mater. **148**, 15 (1995).

[29] A. V. Kobyakov, G. S. Patrin, V. I. Yushkov, Y. G. Shiyan, R. Y. Rudenko, N. N. Kosyrev, and S. M. Zharkov, Magnetic and resonance properties of a low-dimensional cobalt–aluminum oxide–germanium film tunnel junction deposited by magnetron sputtering, Magnetochemistry **8**, 130 (2022).

[30] E. Lundgren, B. Stanka, M. Schmid, and P. Varga, Thin films of Co on Pt(111): Strain relaxation and growth, Phys. Rev. B **62**, 2843 (2000).

[31] J. Thiele, R. Belkhou, H. Bulou, O. Heckmann, H. Magnan, P. L. Fèvre, D. Chandesris, and C. Guillot, EXAFS study of the crystallographic structure of cobalt thin films on pt(111), Surf. Sci. **384**, 120 (1997).

[32] M. Farle, W. Platow, E. Kosubek, and K. Baberschke, Magnetic anisotropy of Co/Cu(111) ultrathin films, Surf. Sci. **439**, 146 (1999).

[33] W. Betteridge, The properties of metallic cobalt, Prog. Mater. Sci. **24**, 51 (1980).

[34] S. H. Ge, C. X. Li, S. S. Li, and Y. D. Zhang, Structures and magnetic properties of co/ta multilayered thin films, Phys. Status Solidi A **132**, 487 (1992).

[35] M. F. Chioncel and P. W. Haycock, Structural characterization of cobalt thin films grown by metal-organic CVD, Chem. Vapor Deposition **11**, 235 (2005).

[36] B. Warren, X-ray studies of deformed metals, Progr. Metal Phys. **8**, 147 (1959).

[37] A. J. C. Wilson, Imperfections in the structure of cobalt II. mathematical treatment of proposed structure, Proc. R. Soc. London A **180**, 277 (1942).

[38] D. M. Donnet, K. M. Krishnan, and Y. Yajima, Domain structures in epitaxially grown cobalt thin films, J. Phys. D **28**, 1942 (1995).

[39] M. Hehn, S. Padovani, K. Ounadjela, and J. P. Bucher, Nanoscale magnetic domain structures in epitaxial cobalt films, Phys. Rev. B **54**, 3428 (1996).

[40] L. Fallarino, S. Stienen, R. A. Gallardo, J. A. Arregi, V. Uhlíř, K. Lenz, R. Hubner, A. Oelschlagel, O. Hellwig, and J. Lindner, Higher-order ferromagnetic resonances in out-of-plane saturated Co/Au magnetic multilayers, Phys. Rev. B **102**, 094434 (2020).

[41] L. Fallarino, A. Oelschlagel, J. A. Arregi, A. Bashkatov, F. Samad, B. Bohm, K. Chesnel, and O. Hellwig, Control of domain structure and magnetization reversal in thick Co/Pt multilayers, Phys. Rev. B **99**, 024431 (2019).

[42] R. Salikhov, F. Samad, S. S. P. Kanth Arekapudi, R. Ehrler, J. Lindner, N. S. Kiselev, and O. Hellwig, Control and tunability of magnetic bubble states in multilayers with strong perpendicular magnetic anisotropy at ambient conditions, Phys. Rev. B **106**, 054404 (2022).

[43] L. Fallarino, O. Hovorka, and A. Berger, Field orientation dependence of magnetization reversal in thin films with perpendicular magnetic anisotropy, Phys. Rev. B **94**, 064408 (2016).

[44] See Supplemental Material at http://link.aps.org/supplemental/10.1103/PhysRevB.108.184429 for the additional measurements on the influence of Si surface miscut, RSM of additional samples, raw FMR spectra and fit, thickness dependence of Ms and $K_{2\perp}$, and hysteresis loop as well as MFM image of 35 nm Co without Pt seed.

[45] ICDD, Cobalt, Powder Diffraction File 4+, 040033863 (2021).

[46] ICDD, Cobalt, Powder Diffraction File 4+, 000150806 (2021).

[47] P. F. Fewster, Reciprocal space mapping, Crit. Rev. Solid State Mater. Sci. **22**, 69 (1997).

[48] S. Gaudet, K. D. Keyser, S. Lambert-Milot, J. Jordan-Sweet, C. Detavernier, C. Lavoie, and P. Desjardins, Three dimensional reciprocal space measurement by x-ray diffraction using linear and area detectors: Applications to texture and defects determination in oriented thin films and nanoprecipitates, J. Vac. Sci. Technol., A **31**, 021505 (2013).

[49] J. Zhang, Z. Sun, J. Sun, S. Kang, S. Yu, G. Han, S. Yan, L. Mei, and D. Li, Structural and magnetic properties of patterned perpendicular media with linearly graded anisotropy, Appl. Phys. Lett. **102**, 152407 (2013).

[50] B. J. Kirby, J. E. Davies, K. Liu, S. M. Watson, G. T. Zimanyi, R. D. Shull, P. A. Kienzle, and J. A. Borchers, Vertically graded anisotropy in Co/Pd multilayers, Phys. Rev. B **81**, 100405(R) (2010).

[51] P. K. Greene, J. Osten, K. Lenz, J. Fassbender, C. Jenkins, E. Arenholz, T. Endo, N. Iwata, and K. Liu, Tuning perpendicular anisotropy gradient in Co/Pd multilayers by ion irradiation, Appl. Phys. Lett. **105**, 072401 (2014).

[52] C. Kittel, On the theory of ferromagnetic resonance absorption, Phys. Rev. **73**, 155 (1948).

[53] M. Farle, Ferromagnetic resonance of ultrathin metallic layers, Rep. Prog. Phys. **61**, 755 (1998).

[54] F. Schreiber, J. Pflaum, Z. Frait, T. Mühge, and J. Pelzl, Gilbert damping and g-factor in FexCo1-x alloy films, Solid State Commun. **93**, 965 (1995).

[55] J. M. Shaw, H. T. Nembach, T. J. Silva, and C. T. Boone, Precise determination of the spectroscopic g-factor by use of broadband ferromagnetic resonance spectroscopy, J. Appl. Phys. **114**, 243906 (2013).

[56] R. Salikhov, L. Reichel, B. Zingsem, R. Abrudan, A. Edström, D. Thonig, J. Rusz, O. Eriksson, L. Schultz, S. Fähler, M. Farle, and U. Wiedwald, Enhanced spin–orbit coupling in tetragonally strained Fe–Co–B films, J. Phys.: Condens. Matter **29**, 275802 (2017).

[57] J. Pelzl, R. Meckenstock, D. Spoddig, F. Schreiber, J. Pflaum, and Z. Frait, Spin orbit-coupling effects on g-value and damping factor of the ferromagnetic resonance in co and fe films, J. Phys.: Condens. Matter **15**, S451 (2003).

[58] Z. Frait, Ferromagnetic resonance of single crystal hexagonal close packed cobalt, Br. J. Appl. Phys. **15**, 993 (1964).

[59] C. Kittel, Theory of the structure of ferromagnetic domains in films and small particles, Phys. Rev. **70**, 965 (1946).

[60] A. Hubert and R. Schäfer, Domain theory, in *Magnetic Domains* (Springer, Berlin, 1998), pp. 99–335.

[61] R. Allenspach and M. Stampanoni, Magnetic domain imaging of epitaxial thin films by spin-polarized scanning electron microscopy, MRS Proc. **231**, 17 (1991).

[62] E. Sallica Leva, R. C. Valente, F. Martínez Tabares, M. Vásquez Mansilla, S. Roshdestwensky, and A. Butera, Magnetic domain crossover in FePt thin films, Phys. Rev. B **82**, 144410 (2010).

[63] J. Brandenburg, R. Huhne, L. Schultz, and V. Neu, Domain structure of epitaxial co films with perpendicular anisotropy, Phys. Rev. B **79**, 054429 (2009).

[64] O. Hellwig, A. Berger, J. B. Kortright, and E. E. Fullerton, Domain structure and magnetization reversal of antiferromagnetically coupled perpendicular anisotropy films, J. Magn. Magn. Mater. **319**, 13 (2007).

[65] K. Bairagi, A. Bellec, V. Repain, C. Fourmental, C. Chacon, Y. Girard, J. Lagoute, S. Rousset, L. LeLaurent, A. Smogunov, and C. Barreteau, Experimental and theoretical investigations of magnetic anisotropy and magnetic hardening at molecule/ferromagnet interfaces, Phys. Rev. B **98**, 085432 (2018).